High Fidelity Simulations and Modelling of Dissipation in Boundary Layers of Non-ideal Fluid Flows

Tosto, Francesco; Wheeler, Andrew; Pini, Matteo

DOI
10.1007/978-3-031-30936-6_7

Publication date
2023

Document Version
Final published version

Published in
ERCOFTAC Series

High Fidelity Simulations and Modelling of Dissipation in Boundary Layers of Non-ideal Fluid Flows

Francesco Tosto[1(✉)], Andrew Wheeler[2], and Matteo Pini[1]

[1] Propulsion and Power, Delft University of Technology, Delft, Netherlands
{f.tosto,m.pini}@tudelft.nl
[2] Whittle Laboratory, University of Cambridge, Cambridge, UK
aw329@cam.ac.uk

Abstract. In this work, we investigate the sources of dissipation in adiabatic boundary layers of non-ideal compressible fluid flows. Direct numerical simulations of transitional, zero-pressure gradient boundary layers are performed with an in-house solver considering two fluids characterized by different complexity of the fluid molecules, namely air and siloxane MM. Different sets of thermodynamic free stream boundary conditions are selected to evaluate the influence of the fluid state on the frictional loss and dissipation mechanisms. The thermophysical properties of siloxane MM are obtained with a state-of-the-art equation of state. Results show that the dissipation due to both time-mean strain field and irreversible heat transfer, and the turbulent dissipation are significantly affected by both the molecular complexity of the fluid and its thermodynamic state. The dissipation coefficient calculated from the DNS is then compared against the one obtained from a reduced-order boundary layer CFD model [1] which has been extended to treat fluids modeled with arbitrary equations of state [7].

Keywords: boundary layer · dissipation coefficient · Non-Ideal Compressible Fluid Dynamics · organic Rankine cycle · Direct Numerical Simulation · turbulence

1 Introduction

The irreversible entropy generation due to viscous processes in boundary layers is one of the main loss mechanisms affecting internal flow devices such as turbomachines or heat exchangers. With regards to turbomachinery, this contribution can account for up to one-sixth of the total loss in a turbine [3]. The share increases in compressors, where the flow becomes more prone to separation due to the presence of adverse pressure gradients over the blade. Fluid flow characteristics strongly affect the viscous dissipation, which depends on the free-stream Reynolds and Mach number, the state of the boundary layer, i.e., laminar or turbulent, and the fluid parameters.

Usually, the rate of entropy generation is estimated with the so-called dissipation coefficient, C_{d}. Unlike the skin friction coefficient C_{f}, which measures the local dissipation at the wall, the dissipation coefficient shows a weak dependence on the boundary layer shape factor and is a good measure of the amount of dissipation occurring

M. White et al. (Eds.): NICFD 2022, ERCOFTAC 29, pp. 62–71, 2023.
https://doi.org/10.1007/978-3-031-30936-6_7

within the boundary layer. Nevertheless, its value strongly depends on the boundary layer regime, i.e., laminar or turbulent. As pointed out by Denton [3] and Schlichting [8], in turbulent boundary layers, the C_d shows a weak dependence on the pressure gradient. Therefore, the turbulent flat plate boundary layer flow still provides good indications of the amount of viscous dissipation.

Although analytical solutions and correlations for both C_f and C_d in boundary layer flows are well established in literature [8,12], little knowledge has been developed on how both the complexity of the molecular structure of fluid and the thermodynamic state of the free-stream flow influence the viscous dissipation and the loss breakdown. Indeed, internal flow devices for process and energy systems such as organic Rankine cycle power system [2] operate with complex organic compounds, often in the supercritical or dense vapor state. Such fluids exhibit strong variations of thermo-physical fluid properties which sensibly affect the development of the boundary layer, the turbulence breakdown, and the dissipation. Direct numerical simulations of dense vapor boundary layer flows [9] have been performed to investigate the turbulence in non-ideal fluid dynamics. However, no simulation in thermodynamic and fluid dynamic conditions of engineering interest, using accurate models for the estimation of the thermo-physical properties of the fluid, has been performed.

In this work, we study the various sources of dissipation in adiabatic boundary layers in zero-pressure gradient non-ideal compressible fluid flows. Direct numerical simulations of transitional, zero-pressure gradient boundary layers are performed with an in-house solver. Two fluids characterized by different levels of complexity of the fluid molecules are considered, namely air and hexamethyldisiloxane (MM). Different sets of thermodynamic free stream boundary conditions are selected to evaluate the influence of the fluid state on the frictional loss and dissipation mechanisms. State-of-the-art equations implemented in a well-known fluid library [6] are used to estimate the thermo-physical properties of siloxane MM. Results are compared against those from a reduced-order model (ROM) code [7] solving the boundary layer equations in transformed coordinates for dense vapors. The final goal of the study is to develop a unified relation for the dissipation coefficient C_d as a function of the Reynolds number, the thermodynamic fluid state, the molecular complexity, and the level of flow compressibility. Such relation can then be used in engineering applications for preliminary estimations of the profile loss in internal flow devices such as turbomachinery or heat exchangers.

2 Theoretical Background

Resolving the small scales of the turbulent flow field through DNS enables the accurate investigation of the dissipation occurring in the vicinity of the wall. According to Hughes and Brighton [4], the losses can be estimated by inspecting the rise in entropy due to irreversible processes. Considering a control volume encompassing the whole boundary layer, the time-mean rate of entropy change is calculated as [11]

$$\int_S \overline{\rho s \mathbf{V}} \cdot \mathrm{d}\mathbf{S} = \int_V \overline{\theta} - \int_S \overline{\left(\frac{\mathbf{q}}{T}\right)} \cdot \mathrm{d}\mathbf{S}, \tag{1}$$

where the overline denotes time-average quantities. The two terms on the right-hand side are the time-average fluxes of entropy and reversible heat transfer across the surfaces. The dissipation is embedded in $\overline{\theta}$ and can be rewritten as

$$\overline{\theta} = \overline{\frac{\Phi}{T} + \frac{\epsilon}{T} + \frac{\zeta}{T}}. \tag{2}$$

The first two terms on the right-hand side constitute the viscous dissipation, which can be further split into a contribution from the mean velocity and strain field, $\overline{\Phi}/T$, and a contribution due to unsteady effects, i.e., the turbulent kinetic energy dissipation, $\overline{\epsilon}/T$. The third term represents the contribution due to irreversible heat transfer. $\overline{\theta}$ can be determined by calculating the instantaneous total dissipation terms ($\Phi/T + \epsilon/T$) and heat flux term (ζ/T) and averaging them over time. The contribution from the time-mean strain, Φ/T, instead, can be computed from the Favre-average flow, and this can then be subtracted from $\Phi/T + \epsilon/T$ to obtain the contribution due to turbulent dissipation. Alternatively, for a boundary layer in equilibrium, $\overline{\Phi}/T$ within the control volume can be obtained by subtracting the time-average turbulence production $\overline{Pr}$ across the boundary layer, defined as

$$\overline{Pr} = -\frac{1}{\rho u_{\mathrm{e}}^3} \int_0^{\delta} \overline{\rho u_i u_j} \frac{\partial \overline{u_i}}{\partial x_j} \mathrm{d}y, \tag{3}$$

and the reversible and irreversible contributions to heat transfer from the entropy flux, in line with Eq. 1. Indeed, for an equilibrium boundary layer, the production term $\overline{P}$ matches the turbulence dissipation, $\overline{\epsilon}$. This second approach is used in this study because the integration of the turbulence production is less mesh sensitive than that of the dissipation terms. Turbulence production is also used to compute the dissipation coefficient, which, for a compressible flow case, reads

$$C_{\mathrm{d}} = \overline{Pr} + \frac{1}{\rho_{\mathrm{e}} u_{\mathrm{e}}^3} \int_0^{\delta} \mu \left(\frac{\partial \overline{u_i}}{\partial x_j} \right)^2 \mathrm{d}y. \tag{4}$$

In this equation, the first term is the contribution to the dissipation due to the turbulent production, which matches the turbulent dissipation in equilibrium boundary layers, while the second one is the contribution due to the time-mean strain field. The dissipation coefficient here takes into account the loss of mechanical energy of the mean flow rather than that of the total mechanical energy, in agreement with the approach used to compute dissipation coefficients with conventional Reynolds-averaged Navier-Stokes solvers.

The C_{d} values obtained from the DNS have been compared against those obtained from a reduced-order model (ROM) solving the two-dimensional boundary layer equations in transformed coordinate and implementing the Cebeci-Smith turbulence model. This model is implemented in *BLnI*, an in-house developed Matlab code. A detailed overview of the ROM, its numerical implementation, and the turbulence model can be found in Refs. [1,7].

3 Methodology

To accurately evaluate the loss breakdown within a non-ideal boundary layer flow, direct numerical simulations of zero-pressure gradient boundary layer flows of air and siloxane MM have been performed. The simulations have been run on *3DNS*, a multi-block structured compressible Navier-Stokes solver for high-performance computations. A technical overview of the solver is provided in Refs. [11].

Three different sets of high-fidelity numerical simulations have been run. Table 1 lists the details of the test cases. All simulations have been performed using a free-stream Mach number of 0.9. The first case simulates the boundary layer flow of air modelled as an ideal gas at standard conditions, i.e., $T_\mathrm{e} = 288$ K and $p_\mathrm{e} = 1$ bar, the subscript e denoting the free-stream conditions. The iMM and niMM cases, instead, refer to simulations of siloxane MM at free-stream thermodynamic conditions close to that of a dilute gas and a dense vapor, respectively. Thermo-physical properties of siloxane MM are calculated using an entropy-based equation of state which is explicit in density and internal energy. This equation has been developed by interpolating fluid property data obtained from accurate Helmholtz energy-based equations of state [6].

Table 1. Test cases evaluated in this study. Free-stream conditions and grid resolution parameters are reported.

	fluid	$p_{\mathrm{r,e}}$	$T_{\mathrm{r,e}}$	Z_e	Ec_e	L_x [m]	H
air	air ideal gas	0.0264	2.182	1	$1.1 \cdot 10^{-3}$	0.023	1.84
iMM	siloxane MM	0.1	1	0.96	$1.5 \cdot 10^{-4}$	$5 \cdot 10^{-3}$	1.45
niMM		1.15	1.05	0.54	$6.8 \cdot 10^{-5}$	$4.42 \cdot 10^{-4}$	1.49
	fluid	x^+	$y^+_{1^{\mathrm{st}}}$	$y^+_{10^{\mathrm{th}}}$	z^+	$n_i \times n_j \times n_k$	
air	air ideal gas	9.06	0.88	9.85	9.06	$2500 \times 800 \times 250$	
iMM	siloxane MM	9.13	0.88	9.85	9.13	$2500 \times 800 \times 250$	
niMM		8.82	0.88	9.85	8.82	$2500 \times 800 \times 250$	

The number of grid points in each direction, as well as the corresponding values of x^+, y^+ at the first cell in the proximity of the wall, and z^+ are reported in Table 1. The plate length is defined to ensure a $Re_L = 5 \cdot 10^5$ for all cases. The corresponding channel height and width are defined as 20% and 10% of the length, respectively. The prescribed height of the domain ensures that the influence of the blockage on the flow is negligible: the measured values of Clauser's beta parameter, defined as

$$\beta_{\mathrm{Cl}} = \frac{\delta^*}{\tau_w} \frac{\mathrm{d}p}{\mathrm{d}x} \tag{5}$$

which takes into account the effect of the pressure gradient on the boundary layer, are within the $-0.15 < \beta_{\mathrm{Cl}} < 0$ range. As a consequence, the mild favourable pressure gradient does not significantly affect the boundary layer development. Stagnation temperature and pressure values are prescribed at the inlet, the static pressure value is instead

prescribed at the outlet. No-slip adiabatic conditions are imposed at the wall. The upper surface is modeled as a free-slip wall, while periodic boundary conditions are imposed in the spanwise direction. To avoid non-physical leading edge effects, a Blasius laminar profile at $Re_x = 10^5$ is introduced at the inlet. The CFL number is unitary. Laminar two-dimensional simulations with the boundary conditions reported in Table 1 are first performed. Solutions from these simulations are then used to initialize the three-dimensional simulations. 3D simulations are performed in the laminar regime for the first 10000 time steps. Then, a trip is triggered at a location x such that $Re_x = 2 \cdot 10^5$.

Statistical averages are performed over the homogeneous spanwise direction and over at least two convective time units based on the free-stream velocity and the axial chord. During the simulations, time-mean flow field and turbulence quantities are calculated by means of a Favre (density-weighted) time-averaging technique.

For comparison, the same cases reported in Table 1 are simulated using the *BLnI* code. However, the free-stream Mach number is here varied to study the effect of compressibility on the overall dissipation. Both laminar, fully turbulent, and transitional regimes are numerically simulated: the transition is imposed at the same location where the trip is introduced in the DNS. The plate length matches that of the numerical simulations, and it is discretized with 200 points in the longitudinal direction. The first grid spacing in the normal-to-wall direction is set to 10^{-5} m for all cases, with a grid expansion factor of 1.02. These values have been proved to ensure grid-independent results. The wall is adiabatic.

4 Results

4.1 Analysis of Dissipation Based on DNS

Figure 1 shows the results of the loss analysis described in Sect. 2 for all the cases listed in Table 1. To avoid nonphysical results due to the flow transition induced by tripping the boundary layer, the rise in irreversible entropy production is computed by integrating over a control volume, where the inlet boundary is located right after the transition point and the outlet one at the given streamwise location. Within this control

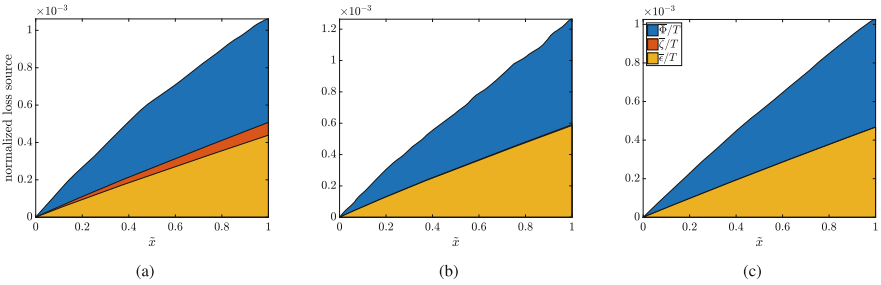

Fig. 1. Dissipation breakdown along the flat plate for the cases (a) *air*, (b) *iMM* and (c) *niMM*. The integration of each contribution is performed from $\tilde{x} = 0$ to $\tilde{x} = 1$, where $\tilde{x} = (x - x_{tr})/(L_x - x_{tr})$.

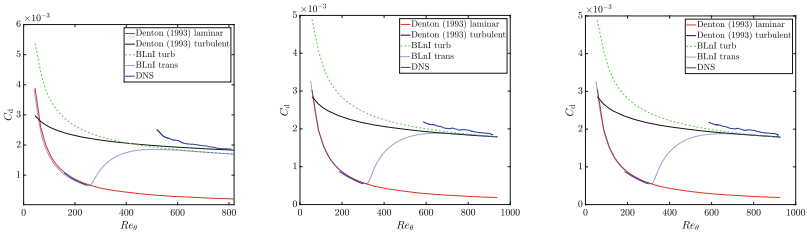

Fig. 2. Dissipation coefficient C_d *vs* Re_θ for the cases (a) *air*, (b) *iMM* and (c) *niMM*. Results from turbulent and transitional simulations conducted with *BLnI* as well as those obtained from the DNS are plotted. Correlations by Denton and Schlichting are also displayed.

volume, the boundary layer is assumed to have reached an equilibrium state. No major differences are observed between the *iMM* and *niMM* cases: a relatively higher dissipation due to the time-mean strain field is observed for the *niMM* case, arguably due to the higher value of dynamic viscosity that siloxane MM exhibits in the dense vapor state. The contribution due to irreversible heat transfer is negligible in both cases. In the case of air, instead, such contribution becomes non-negligible; however, it remains an order of magnitude lower than the other two contributions. Indeed, in perfect gases, the heat generated by the dissipation of the turbulent kinetic energy at the smallest scales induces variations of thermo-physical properties larger than those occurring in fluid characterized by high molecular complexity such as siloxane MM.

4.2 Comparison DNS-ROM

Figure 2 shows the trend of the dissipation coefficient with Re_θ computed for the cases of Table 1. The results of the fully turbulent and transitional simulations conducted with *BLnI* are also displayed. Trends of C_d as provided by the empirical correlations of Schlichting [3,8] for the laminar and turbulent incompressible cases are also plotted for comparison.

In the laminar regime, the dissipation coefficient calculated from the DNS results qualitatively matches the trend predicted by means of both the empirical and the reduced-order model. The maximum deviation between the values predicted by DNS and by the correlation is of the order of 2%. In the turbulent regime, the trend of C_d approaches that of the incompressible Schlichting correlation for both the three cases in the proximity of the trailing edge of the plate. The $C_\mathrm{d} - Re_\theta$ trend in the proximity of the tripping point is not reported due to non-physical trends in that region. For the sake of clarity, the three solutions are reported in Fig. 3b. The lowest value of C_d in the turbulent regime is found for the case of air when $Re_\theta > 800$, suggesting that fluids made by simple molecules exhibit reduced values of dissipation at fixed M_e and Re_θ. The trend can also be explained by inspecting the value of the freestream Eckert number, which is inherently lower for dense vapor flows. As a consequence, in fluids made by complex molecules in both the ideal and the non-ideal thermodynamic state, the thermal and kinetic fields are decoupled [9,10] irrespective of the freestream Mach

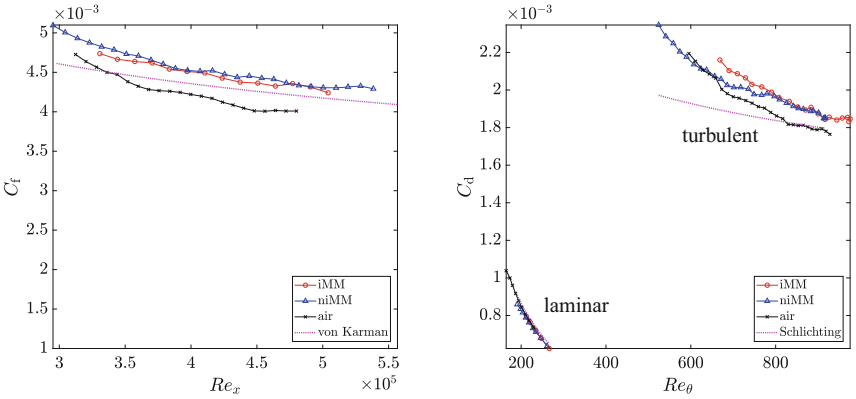

Fig. 3. (a) Skin friction coefficient *vs* Re_x and (b) dissipation coefficient *vs* Re_θ for all the cases of Table 1. Trends obtained from empirical correlations are also plotted for comparison.

number, resembling the physical behavior of an incompressible flow. This result is in line with those obtained by [7] for adiabatic laminar boundary layers of dense vapors at $M_\mathrm{e} = 2$. Figure 3a shows the trend of the skin friction coefficient C_f for all the three investigated cases. Trends are qualitatively in agreement with those obtained for the dissipation coefficient C_d. According to Schlichting, for a zero-pressure gradient boundary layer flow in equilibrium, the relation between the dissipation and the skin friction coefficient is

$$C_\mathrm{d} = \frac{C_\mathrm{f}}{2}\frac{H^*}{2}, \tag{6}$$

where $H^* = \theta^*/\theta$ is the energy shape factor, being θ^* and θ the kinetic energy and momentum thicknesses, respectively. In the turbulent flow region, $H^* \sim 1.774$ for all cases, which is in line with the values computed by Jardine [5]; as a consequence, changes in the dissipation coefficient between the three cases are solely due to changes in the value of the skin friction coefficient.

Figure 4a shows the velocity profiles in wall units evaluated at a x location corresponding to $Re_\theta = 800$, while Fig. 4b depicts the compressible van-Driest velocity profile as a function of the y^+ evaluated at the same location. Results from the *BLnI* code evaluated at the same Re_θ are also reported. No major deviation from the law of the wall trend is observed for all cases in neither the viscous sublayer, the buffer zone, where the peak in turbulence production is observed (see Fig. 5a), and the logarithmic region. However, in the buffer zone and the logarithmic region, the trends obtained from the ROM do not collapse over those of the DNS. The larger deviation from the DNS trend is measured for the *air* case, where the relative difference in the u^+ value at $y^+ = 40$ is 10%. Such deviation decreases if van-Driest velocity profiles are considered: for the *air* case, at $y^+ = 40$, the relative difference is 7%. Although $M_\mathrm{e} = 0.95$ for all the three cases, results obtained by applying the van Driest transformation do not show any major deviation from the $u^+ - y^+$ trend of Fig. 4a. The turbulence production is almost insensitive to the fluid molecular complexity and the thermodynamic state, which peaks at $y^+ \sim 10$ for all three cases.

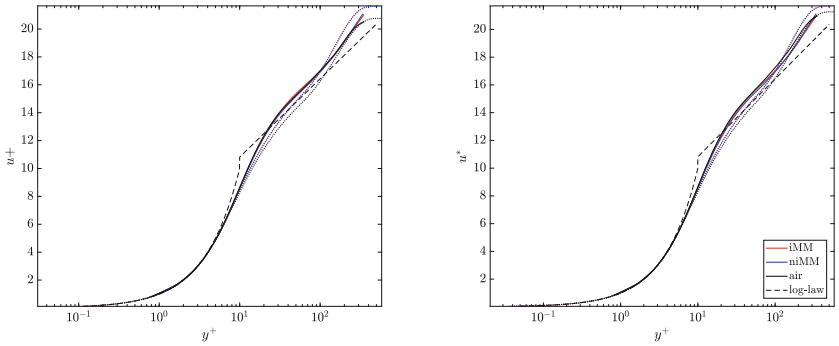

Fig. 4. Velocity profiles in (a) wall coordinates and (b) van Driest transformed coordinates. Continuous lines denote the trends obtained from the DNS, whereas dotted ones denote those obtained from the ROM. Black dashed lines denote the linear and logarithmic laws, with $k = 0.41$ and $C = 5.2$

Figure 5b displays the enthalpy profiles within the boundary layer evaluated at a x location corresponding to $Re_\theta = 800$. Results obtained from both the DNS and the ROM are plotted. It can be noted that the enthalpy increase close to the wall strongly depends on both the fluid molecular complexity and the thermodynamic fluid state. In particular, the enthalpy difference between the wall and the freestream is maximum in the case of air, while the boundary layer of siloxane MM can be assumed almost isothermal in both thermodynamic conditions. This finding is inherently related to the high heat capacity of the organic fluid, which enables to store thermal energy using the many degrees of freedom of the molecule. Among the three cases, the *niMM* case shows a nearly flat enthalpy profile, due to the increasingly high c_p in the dense vapor state.

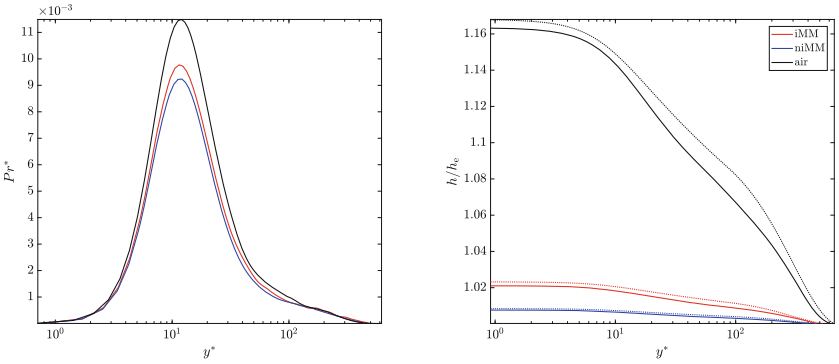

Fig. 5. (a) Normalized turbulence production $Pr^* = Pr \cdot \delta/(\rho V_e^3)$ *vs* y^+. (b) Enthalpy profiles for all the cases of Table 1. Continuous lines denote the trends obtained from the DNS, whereas dotted ones denote those obtained from the ROM. The trends have been evaluated at a location where $Re_\theta = 800$.

Furthermore, the temperature profile strongly affects the value of the dissipation coefficient. Using the Falkner-Skan variable transformation, one can write, for a turbulent flow,

$$C_{\mathrm{d}} = \frac{1}{\sqrt{Re_x}} \int_0^{\eta_{\mathrm{e}}} CR_{\mathrm{turb}} \frac{T_{\mathrm{e}}}{T} \tilde{v}^2 \mathrm{d}\eta, \tag{7}$$

where $CR_{\mathrm{turb}} = \rho(\mu + \mu_\tau)/(\rho_{\mathrm{e}}\mu_{\mathrm{e}})$ takes into account also the eddy viscosity μ_τ. At a fixed Reynolds number, for an ideal gas, variations of T_{e}/T prevail over those of CR_{turb}, thus leading to a reduction of the C_{d} value for simple fluid molecules in the compressible flow regime.

Although a mismatch is observed, the trends obtained with the *BLnI* code are qualitatively in agreement with those obtained from the high-fidelity numerical simulations. This corroborates the hypothesis that the ROM, coupled with an algebraic turbulence model, is sufficiently accurate to preliminary estimate the dissipation rate occurring in laminar and turbulent boundary layers.

5 Conclusion

Direct numerical simulations of zero-pressure gradient boundary layer flow of air and siloxane MM operated in both the dilute gas and dense vapor state have been performed. All sources of dissipation have been discerned and analyzed. The trend of the skin friction and dissipation coefficient as a function of the Reynolds number, as well as those of the velocity and temperature profiles, have been discussed and compared against those obtained from a reduced order model implemented in an in-house code which solves the two-dimensional turbulent boundary layer equations in transformed coordinates. Based on the results obtained from the work, the following conclusions can be drawn.

1. At fixed Reynolds number, turbulent boundary layer flows of fluids made of complex molecules exhibit a higher value of both the skin friction and the dissipation coefficients than those of air. This is due to the decoupling between thermal and kinematic fields.
2. Regardless of the fluid thermodynamic state, turbulent boundary layer flows of complex molecules fluids are almost isothermal.
3. The loss contribution due to irreversible heat transfer is negligible in flows of fluids made of high molecular complexity.

Future works will investigate more in detail the structure of density and pressure fluctuations in ideal gas and dense vapor boundary layers. Other fluids other than air and siloxane MM will also be investigated with the ROM, as well as the effect of favorable and adverse pressure gradients. The final aim is to fully characterize the dissipation within boundary layer flows of dense vapors to accurately predict losses in non-conventional turbomachinery.

Acknowledgement. The authors acknowledge the contribution of dr. Carlo de Servi, dr. Adam J. Head, Dominic Dijkshoorn, and Federico Pizzi to the development and verification of the reduced-order model. This research has been supported by the Applied and Engineering Sciences Domain (TTW) of the Dutch Organization for Scientific Research (NWO), Technology Program of the Ministry of Economic Affairs, grant # 15837.

References

1. Cebeci, T.: Convective Heat Transfer. Number v. 2 in Convective Heat Transfer. Horizons Publishing (2002)
2. Colonna, P., et al.: Organic rankine cycle power systems: from the concept to current technology, applications, and an outlook to the future. J. Eng. Gas Turbines Power **137**(10), 100801 (2015)
3. Denton, J.D.: Loss mechanisms in turbomachines. In: Volume 2: Combustion and Fuels; Oil and Gas Applications; Cycle Innovations; Heat Transfer; Electric Power; Industrial and Cogeneration; Ceramics; Structures and Dynamics; Controls, Diagnostics and Instrumentation; IGTI Scholar Award, Cincinnati, Ohio, USA, p. V002T14A001. American Society of Mechanical Engineers (1993)
4. Hughues, W.F., Brighton, J.A.: Fluid Dynamics (Schaum's Outline Series), 2nd edn. McGraw-Hill, New York (1983)
5. Jardine, L.J.: The Effect of Heat Transfer on Turbine Performance, p. 185
6. Lemmon, E.W., Bell, I.H., Huber, M.L., McLinden, M.O.: NIST standard reference database 23: reference fluid thermodynamic and transport properties-REFPROP, version 10.0, National Institute of Standards and Technology (2018)
7. Pini, M., De Servi, C.: Entropy generation in laminar boundary layers of non-ideal fluid flows. In: di Mare, F., Spinelli, A., Pini, M. (eds.) NICFD 2018. LNME, pp. 104–117. Springer, Cham (2020). https://doi.org/10.1007/978-3-030-49626-5_8
8. Schlichting, H., Gersten, K.: Boundary-Layer Theory, 9th edn. Springer, Heidelberg (2016). https://doi.org/10.1007/978-3-662-52919-5
9. Sciacovelli, L., Gloerfelt, X., Passiatore, D., Cinnella, P., Grasso, F.: Numerical investigation of high-speed turbulent boundary layers of dense gases. Flow Turbulence Combust **105**(2), 555–579 (2020)
10. Tosto, F., Lettieri, C., Pini, M., Colonna, P.: Dense-vapor effects in compressible internal flows. Phys. Fluids **23**, 086110 (2021)
11. Wheeler, A.P.S., Sandberg, R.D., Sandham, N.D., Pichler, R., Michelassi, V., Laskowski, G.: Direct numerical simulations of a high-pressure turbine vane. J. Turbomach. **138**(7) (2016)
12. White, F.M., Majdalani, J.: Viscous Fluid Flow, vol. 3. McGraw-Hill, New York (2006)